

## PAPER • OPEN ACCESS

# Gamma Efficiency Simulations towards Coincidence Measurements for Fusion Cross Sections

To cite this article: M. Heine *et al* 2016 *J. Phys.: Conf. Ser.* **763** 012005

View the [article online](#) for updates and enhancements.

## Related content

- [Classical electron ionization cross sections](#)  
A E Kingston
- [On the high-energy behaviour of electron capture cross sections](#)  
J P Coleman
- [Coincidence measurements of electron impact excitation of the  \$4^1P\_1\$  state of Zn](#)  
M Piwiski, Kosowski, D Dziczek *et al.*

## Recent citations

- [Sub-barrier fusion cross section measurements with STELLA](#)  
M. Heine *et al*
- [Cross section measurements in the  \$^{12}\text{C}+^{12}\text{C}\$  system](#)  
S. Courtin *et al*



## IOP | ebooks™

Bringing together innovative digital publishing with leading authors from the global scientific community.

Start exploring the collection—download the first chapter of every title for free.

# Gamma Efficiency Simulations towards Coincidence Measurements for Fusion Cross Sections

M. Heine<sup>1</sup>, S. Courtin<sup>1,2</sup>, G. Fruet<sup>1</sup>, D.G. Jenkins<sup>3</sup>, D. Montanari<sup>1,2</sup>,  
L. Morris<sup>3</sup>, P.H. Regan<sup>4,5</sup>, M. Rudigier<sup>4</sup>, D. Symochko<sup>6</sup>

<sup>1</sup> IPHC-CNRS/Université de Strasbourg, 67037 Strasbourg, (France)

<sup>2</sup> USIAS/Université de Strasbourg, 67083 Strasbourg, (France)

<sup>3</sup> University of York, YO10 5DD York (UK)

<sup>4</sup> University of Surrey, GU2 7XH Guildford (UK)

<sup>5</sup> National Physical Laboratory, TW11 0LW Teddington, Middlesex (UK)

<sup>6</sup> IKP/TU Darmstadt, 64289 Darmstadt, (Germany)

E-mail: marcel.heine@iphc.cnrs.fr

**Abstract.** With the experimental station STELLA (STELLar LABoratory) we will measure fusion cross sections of astrophysical relevance making use of the coincident detection of charged particles and gamma rays for background reduction. For the measurement of gamma rays from the de-excitation of fusion products a compact array of 36 UK FATIMA LaBr<sub>3</sub> detectors is designed based on efficiency studies with Geant4. The photo peak efficiency in the region of interest compares to other gamma detection systems used in this field.

The features of the internal decay of <sup>138</sup>La is used in a background study to obtain an online calibration of the gamma detectors. Background data are fit to the Monte Carlo model of the self activity assuming crude exponential behavior of external background. Accuracy in the region of interest is of the order of some keV in this first study.

## 1. Introduction

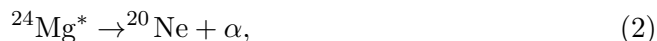
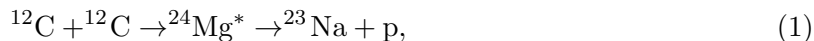
The measurement of sub-barrier light heavy-ion fusion cross sections can yield both insights into nuclear cluster effects [1] and the *S*-factor at energies of astrophysical interest. In particular, <sup>12</sup>C+<sup>12</sup>C was identified as a key reaction on the production route of heavier elements in massive stars during the carbon burning phase [2], in type Ia supernovae and in superbursts from accreting neutron stars. Though dedicated measurements of sub-barrier <sup>12</sup>C+<sup>12</sup>C cross sections were carried out since the late 1960's, no comprehensive experimental data around the energy regime of astrophysical interest are available at the time being. Hence, the input rates to the nucleosynthesis calculations are uncertain by up to two orders of magnitude for <sup>12</sup>C fusion [3].

Since deep sub-barrier fusion reactions are strongly hindered by Coulomb repulsion, the experimental determination of these cross sections, that are expected to be as small as nano barn, is highly challenging. In this configuration the reaction channels are orders of magnitude smaller than background contributions [5] and additional experimental effort is made to determine the fusion cross sections with sufficient accuracy. In the STELLA project described in detail in [4] the determination of such cross sections is targeted with coincidence measurements using the so called gamma-particle-technique [5] based on the time correlated determination of charged particle and gamma energies as well as the measurement of their angular distributions. In



addition, the experimental station will be equipped with a rotating target mechanism for sufficient heat dissipation to sustain  $^{12}\text{C}$  beam intensities of up to  $10\mu\text{A}$

For sub-barrier fusion of the  $^{12}\text{C}+^{12}\text{C}$  system the reaction channels, that include light charged particles, are



with  $Q_{\text{p}} = 2.24$  MeV and  $Q_{\alpha} = 4.62$  MeV. The reaction channel with a  $^{23}\text{Mg}$  fragment and neutron emission cannot be accessed for relative energies below  $Q_{\text{n}} = -2.6$  MeV. The population of the final state of  $^{24}\text{Mg}$  with  $Q_{\gamma} = 13.93$  MeV *via* gamma emission is weak by phase space arguments and indeed the yield was found to be negligible in previous studies at higher relative energies [6]. It was furthermore shown that the major deexcitation radiation of the reactions (1) and (2) cascades through the first excited states of the fragment nuclei [7], and hence the detection of characteristic gamma lines at 440 keV and 1634 keV for the identification of the proton and alpha channel, respectively, is targeted in the first instance.

In section 2 the Geant4 simulations for the optimization of the gamma efficiency are addressed and in section 3 a model for the simulation of the self-activity as well as the fit to experimental data are introduced. The contribution is summarized in section 4.

## 2. Gamma Efficiency Simulations

In order to obtain the highest photo peak efficiency in the gamma detection, comprehensive simulations are carried out for the response to isotropic gamma emission at the target position. For the arrangement of the UK FATIMA LaBr<sub>3</sub> crystals [8, 9], detector configurations in a spherical setup, a cylindrical setup where all detectors are facing the beam line, and a simple pile along the direction of the beam are studied. The detectors are stapled starting from 2.5 cm below the equator of the dome of the target chamber in the horizontal plane containing the beam line and the target (see figure 2 in [4]). For efficiency optimization the closest configuration of detectors with spacing smaller 0.2 cm is set. The positions in the lowest line or ring define the entire structure, because going upwards detectors are placed in the gaps of the lower ones. In general, the geometrical acceptance of the single detectors drops by up to 60% towards higher positions with respect to the beam line, because of the target location 2.5 cm below the center of the dome. In this study ten or twelve detectors in the lowest line or ring are considered in order to take shielding effects as well as clustering of energy depositions into account. In table 1 the acceptance of the above mentioned stapling schemes in percent are comprised. Note that

**Table 1.** Geometrical acceptance in percent of detector alignments in a spherical, cylindrical and wall-like (pile) configuration with ten or twelve detectors in the lowest line or ring.

# Det.	Acceptance [%]		
	Sphere	Cylinder	Pile
10	23.3	23.1	20.6
12	24.4	23.2	21.2

in the spherical setup only 33 and 35 detectors can be placed in the stapling starting with ten or twelve low detectors, respectively. As can be see from table 1, the geometrical acceptance of the pile is significantly lower such that this alignment is ruled out.

The arrangement of ten detectors in the lowest line or ring is less sensitive to additional material like connectors that will be inserted in the beam line and hence this configuration is favored over the configuration with twelve detectors in the lowest segment. The difference of

the geometrical acceptance then is negligible (see table 1) and the so called cylindrical setup is constructed. As can be seen in figure 2 in [4], the distance of every second line is optimized with respect to the beam line to cover the upper hemisphere of the experimental station in the most efficient way.

The distance of all pairs of crystals is analyzed to obtain a measure on the geometry independently from the simulation. The parameters of these distributions reflecting the compactness of the detector placement are shown in table 2, where the mean values and the

**Table 2.** Parameters of the distributions of the pair-wise distance between crystals the spherical as well as cylindrical  $\text{LaBr}_3$  placement with ten or twelve detectors in the lowest ring or line.

Setup	# Det	Mean [cm]	RMS [cm]
sphere	10	18.3	6.6
sphere	12	18.6	6.9
cylinder	10	19.5	7.2
cylinder	12	20.4	7.8

Root Mean Squares (RMS) in cm are listed. As can be seen, the trend found in the simulation is reproduced and in general the spherical configurations are more compact. Note that all distances are given the same weight. Greater distances in the cylindrical setup can be attributed to detectors with lower geometrical acceptance, *i.e.* lower contribution to (and weight in) the geometrical acceptance in table 1. Hence, the cylindrical contributions appear slightly more disadvantageous in the picture of the pair-wise distances.

For the physics interpretation of experimental data here the photo peak efficiency is of interest. It expresses the percentage of gamma rays depositing their entire energy in the detector volume and is shown in figure 1 in comparison to the experimental performance of the  $4\pi$  germanium

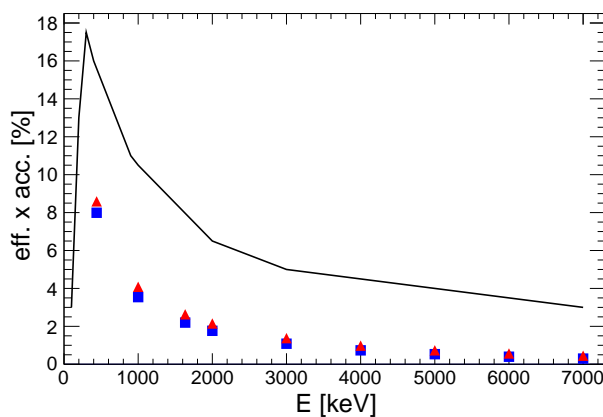


**Figure 1.** [color online] Comparison of the photo peak response to isotropic gamma emission from the target position with different addback situations (red triangles and blue squares: details in the text) in comparison to the GAMMASPHERE array [10] (black line).

detector array GAMMASPHERE [10, 11] (black line). The current simulation is run with an empty target chamber, since the effect of absorption due to detector material and interior supporting structures is expected to be as low as a few percent of the total photo peak response. All relevant elements of the beam line and required connectors as well as supporting structure in this area are included.

Simulated data shown in figure 1 are analyzed summing up all energy depositions to obtain the total photo peak efficiency (red triangles) and on the other hand summing up the photo

peak efficiency of each detector (blue squares). This approach is expected to benchmark the performance of the reconstruction of the gamma ray energies at experimental conditions. As can be seen, the photo peak efficiency is about 3.5% at  $E_\gamma = 1000$  keV and above 30% of the performance of GAMMASPHERE for energies below 2000 keV. This is the relevant energy region for the identification of characteristic gamma rays from the first excited states in the evaporation residue  $^{23}\text{Na}$  and  $^{20}\text{Ne}$  with  $E_\gamma = 440$  keV and  $E_\gamma = 1634$  keV, respectively.

### 3. Internal Activity Simulation

The lanthanum halides crystals are characterized by both excellent scintillation properties and intrinsic activity. The self activity originates from the radioactive isotope  $^{138}\text{La}$  as well as contamination with the chemically equivalent isotope  $^{224}\text{Ac}$  and its decay products. The latter component and its daughter nuclei emit alpha particles of various energies that manifest in gamma ray equivalent energies between  $E = 1600$  keV and  $E = 3000$  keV [12]. The self activity may seriously effect the analysis of low counting rate gamma ray measurements, while the coincidence with charged particles required in the (bigger) frame of this work is expected to completely eliminate this background contribution [5]. However, the study of the  $^{138}\text{La}$  decay outlined in the following paragraphs serves a better characterization of the  $\text{LaBr}_3$  detectors in the simulation. In addition, the pattern of the  $^{138}\text{La}$  decay is used to progress towards an online calibration of the gamma detectors.

The half live of  $^{138}\text{La}$  is  $1.05 \cdot 10^{11}$  yr and the natural abundance is 0.0902% [13]. This introduces a background of around 90 Bq in the  $\text{LaBr}_3$  crystals sized 1.5''x 2.0'' in diameter and length. The decay happens in 66.4% by electron capture (EC) into  $^{138}\text{Ba}$  and in 33.6% by beta decay into  $^{138}\text{Ce}$ . In both cases exclusively the first excited state ( $2^+$ ) is populated leading to prompt gamma ray emission for deexcitation to the ground state ( $0^+$ ) [13]. Hence, the EC and the beta decay transitions are accompanied by gamma rays with energies  $E_\gamma = 1436$  keV and  $E_\gamma = 789$  keV, respectively. Moreover, the  $Q$ -values in the  $^{138}\text{La}$  decay are  $Q_{\text{EC}} = 1738$  keV and  $Q_\beta = 1044$  keV.

The end point energy of the beta decay spectrum into  $^{138}\text{Ce}$  is  $E_\beta = 258$  keV. In the present case the spectral shape is taken from a coincidence measurement described in [14]. It differs significantly from the theoretical calculation (second forbidden Gamow-Teller transition) for energies below 75 keV, but yields the best description of the shape of experimental data in the present work. As discussed in [14], this deviation may be sought with a careful evaluation of the screening factor in the theoretical calculation.

For the description of the decay into  $^{138}\text{Ba}$  electron capture from the  $K$  and  $L$  shell are processed in the simulation with subsequent  $x$ -ray emission. The EC probabilities are taken from [15] and the energies of the edges of the  $K$  and  $L$  shell from [16]. Effects of higher order EC amount to less than 9% and are not taken into account. The  $K\alpha$ ,  $K\beta$  as well as  $L$  shell  $x$ -ray intensities and energies for barium are taken from [17] for the atomic deexcitation implementation. In summary, the gamma ray with  $E_\gamma = 1436$  keV from the first excited state in  $^{138}\text{Ba}$  and characteristic  $x$ -rays occupying the vacancies from the electron captures are generated in this decay branch. This results in a significantly broader distribution around the photo peak of the gamma ray with energy depositions up to 1473 keV where both the gamma- and the  $x$ -ray are detected. In general, two major peaks can be identified [18] and the lower contribution in commonly referred as the  $x$ -ray escape peak.

The simulation is fitted to an experimental background spectrum of a  $\text{LaBr}_3$  detector sized 3.0''x 3.0'' in diameter and length. As a crude approximation a simple exponential function is chosen to account for room background and subtracted from experimental data as shown in figure 2, in the fit to the simulated  $^{138}\text{La}$  decay scheme (blue curve). The present fit is shown as the green curve that is to be compared with the simulation in blue. The range of the fit covers all features of the  $^{138}\text{La}$  decay and the agreement of this first approach with experimental data

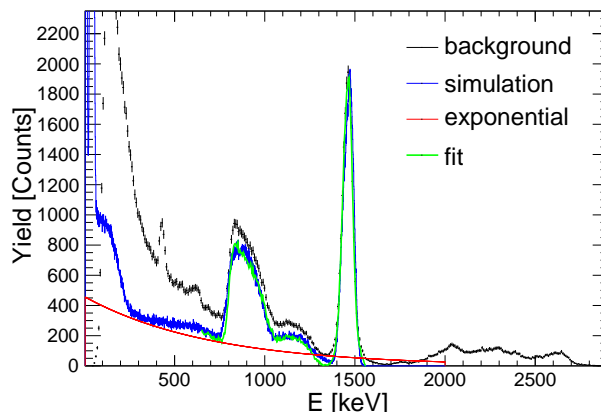


**Figure 2.** [color online] The fit (green curve) of the simulated decay scheme of  $^{138}\text{La}$  (blue curve) to an experimental background spectrum (black crosses), where an exponential (red curve) is subtracted.

motivates further investigation. For energies between  $E = 1600$  keV and  $E = 2800$  keV a broad contribution from alpha particles emitted in the  $^{224}\text{Ac}$  decay chain can be seen in the spectrum. The accretion of this impurities during the production of the crystals may differ from detector to detector and the description of this feature is beyond the scope of the present simulations.

The contribution at around  $E = 430$  keV in figure 2 may be interpreted as the double escape peak from  $^{40}\text{K}$  ( $E_\gamma = 1461$  keV) in the borosilicate glass of the entrance window of the PM tube [18]. This would also imply a contribution around the energy region of the higher gamma line from the  $^{138}\text{La}$  decay. Nominally, the double escape peak should appear at  $E = 439$  keV and the mismatch hints on non-linear response of the  $\text{LaBr}_3$  detectors towards low energy depositions [19]. Further analysis will include the characterization and correction of the energy response of the detectors as well as the simulation of the  $^{40}\text{K}$  decay from the PM tube for the fit shown in figure 2.

For the simulation of the  $^{138}\text{La}$  decay detailed physics input is distributed to the simulation, that reproduces the detector response to the decay features. Hence, in figure 2 also the peak positions of raw experimental data (in channels) are fitted to the simulation for instant calibration (in energy units). The performance is cross checked with  $^{22}\text{Na}$  and  $^{137}\text{Cs}$  runs, where the full energy depositions as well as the associated annihilation peak in the case of  $^{22}\text{Na}$  ( $E_{cal}$ ) are compared with the nominal values ( $E_{nom}$ ). The result is given in table 3. The relative

**Table 3.** Comparison of the nominal peak positions  $E_{nom}$  with the mean energy values from the instant calibration  $E_{cal}$  utilizing characteristic lines from  $^{22}\text{Na}$  and  $^{137}\text{Cs}$  calibration sources. The uncertainty in percent is denoted by  $\Delta$  (see text for details).

$E_{nom}$ [keV]	$E_{cal}$ [keV]	$\Delta$ [%]
511	$526.0 \pm 0.2$	$2.9 \pm 0.2$
662	$672.7 \pm 0.2$	$1.6 \pm 0.2$
1274	$1270.5 \pm 0.8$	$0.2 \pm 0.8$

uncertainty defined by  $\Delta = |(E_{nom} - E_{cal})/E_{nom}|$  is in the order of a few percent. However, we aim for an absolute precision of 1 keV of the instant calibration for gamma energies between  $E = 400$  keV and  $E = 1800$  keV. To achieve this, the energy response of the  $\text{LaBr}_3$  detectors will be characterized in  $^{152}\text{Eu}$  runs and taken into account in the fit routine accordingly. Secondly, the origin of the classified  $^{40}\text{K}$  contribution is investigated with dedicated simulations to obtain

a reliable description of experimental data in the low energy region as well. In the end, the overall agreement of simulation and experiment in a given energy range will define the precision of the online calibration.

#### 4. Summary

For the gamma detection in the STELLA station 36 LaBr<sub>3</sub> crystals sized 1.5''x2.0'' will be utilized. The positioning of the detectors in the hemisphere above the target chamber is optimized utilizing Geant4 simulations. Arrangements of spherical, cylindrical, and pile stack configurations are discussed in terms of the geometrical acceptance and the photo peak efficiency. In the cylindrical setup with ten detectors in the lowest line the geometrical acceptance is 23.1% and the photo peak efficiency at  $E = 1$  MeV is around 3.5%. The results are backed by the calculation of pair-wise distance distributions reflecting the characteristics of the detectors arrangements from the simulations.

Based on the activity of <sup>138</sup>La the performance of the current simulation is tested qualitatively. This comprises the description of the interactions of electrons and gamma rays with the scintillating material as well as the detector geometry implementation. The experimental background spectrum of a 3''x3'' LaBr<sub>3</sub> crystal, that is dominated by the <sup>138</sup>La decay, is reproduced in the energy range between  $E = 650$  keV and  $E = 1650$  keV with a general exponential to account for exterior background sources. The fit is also used for an instant calibration of the gamma detectors for the STELLA-FATIMA project and the absolute uncertainty of the online energy calibration routine is 15 keV in this first approach.

#### Acknowledgments

This work was supported by the IdEx Attractivity grant (F) of the University of Strasbourg, by the STFC (UK) grant number ST/L005743/1, and by the DFG (GER) through grant SFB 1245.

#### References

- [1] Jenkins D G and Courtin S 2015, *Phys. Jour. G* **42**, 034010
- [2] Chieffi A, Limongi M and Straniero O 1998, *ApJ*, **502**, 737
- [3] Gasques L R, Brown E F, Chieffi A, Jiang C L, Limongi M, Rolfs C, Wiescher M and Yakovlev D G 2007, *PRC* **76**, 3, 035802
- [4] Courtin S *et al.* 2016, NIC2016, accepted *JPS Conf. Proc.*
- [5] Jiang C L *et al.* 2012, *NIM A* **682**, 12
- [6] Patterson J R, Winkler H and Zaidins C S 1969, *APJ* **157**, 367
- [7] Erb K A, Betts R R, Korotky S K, Hindi M M, Tung P P, Sachs M W, Willett S J and Bromley D A 1980, *PRC* **22**, 22
- [8] Roberts O J, Bruce A M, Regan P H, Podolyák Z, Townsley C M, Smith J F, Mulholland K F and Smith A 2014, *NIM A* **748**, 91
- [9] Lorusso G *et al.* 2016, *Appl. Rad. Iso.* **109**, 507
- [10] Lauritsen T 2016, <<http://www.phy.anl.gov>>
- [11] Lee I Y 1990, *Nucl. Phys. A* **520**, 641c
- [12] Milbrath B D, Runkle R C, Hossbach T W, Kaye W R, Lepel E A, McDonald B S and Smith L E 2005, *NIM A* **547**, 504
- [13] Firestone R B and Shirley V S 1997, *Table of Isotopes*, (Wiley)
- [14] Quarati F G A, Khodyuk I V, van Eijk C W E, Quarati P and Dorenbos P 2012, *NIM A* **683**, 46
- [15] Bé M M *et al.* 2010, *Monographie BIPM* **5**, Table of Radionuclides, (BIPM)
- [16] Deslattes R D, Kessler Jr. E G, Indelicato P, de Billy L, Lindroth E and Anton J 2003, *Rev. Mod. Phys.* **75**, 35
- [17] Chu S Y F, Ekström L P and Firestone R B 2016, *The Lund/LBNL Nuclear Data Search*, <<http://nucleardata.nuclear.lu.se/toi/index.asp>>
- [18] Camp A, Vargas A and Fernández-Varea J M 2016, *Appl. Rad. Iso.* **109**, 512
- [19] Giaz A *et al.* 2013, *arXiv* 1308.6085